Electronic Supplementary Material (ESI) for Materials Advances.

Supplementary information for Defect tolerant device geometries for lead-halide perovskites

Basita Das[1], Zhifa Liu[1], Irene Aguilera[1], Uwe Rau[1] and Thomas Kirchartz[1,2]
[1]IEK5-Photovoltaik, Forschungszentrum Jülich, 52425 Jülich, Germany
[2]Faculty of Engineering and CENIDE, University of Duisburg-Essen, Carl-Benz-Str. 199, 47057 Duisburg, Germany

Multiphonon capture coefficients

The electron and hole capture coefficients used in Fig 2, 4 -5 are obtained from the generalized model of multiphonon capture described in a previous publication[1] and is also summarized in Table I. The values of electron and hole capture coefficients for donor defect levels at different values of energy in MAPI obtained from the model is also given in Table II.

Table I Generalized microscopic model for calculating multiphonon capture coefficients of defects.

Expressions for quantum defect model that describes the connection between depth of a defect and the radius of the defect wavefunction[2,3]		
Quantum defect parameter (υ_T)	$\upsilon_T = \sqrt{R_{H^*}/\Delta E_{min}} = \frac{1}{\epsilon_\infty}\sqrt{\frac{m^* q^4}{32\pi^2 \Delta E_{min}}}$	(1)
Radius of the deep defect wavefunction (R_T)	$R_T = \frac{a_H^* \upsilon_T}{2}$	(2)
Expressions for calculation of non-radiative multiphonon capture coefficients[4–6]		
Non-radiative multiphonon capture coefficient	$k_{n/p} = \frac{M_{i,f}^2\sqrt{2\pi}}{\hbar^2\omega_\nu\sqrt{l\sqrt{1+x^2}}}\exp\left[l\left(\frac{\hbar\omega_\nu}{2k_B T}+\sqrt{1+x^2}\right.\right.$ $\left.\left.-\ x\cosh^{-1}\left(\frac{\hbar\omega_\nu}{2k_B T}\right)-\ln\left(\frac{1+\sqrt{1+x^2}}{x}\right)\right)\right]$	(3)
No. of phonons emitted during multiphonon transition	$l = \frac{\Delta E}{\hbar\omega_\nu}$	(4)
Multiphonon transition matrix element	$\left\|M_{i,f}\right\|^2 = V_T(l\hbar\omega_\nu)^2$	(5)
Volume of the defect V_T	$V_T = \frac{4}{3}\pi R_T^3$	(6)
Parameter x	$x = \begin{cases} \frac{S_{HR}}{l\sinh(\hbar\omega_\nu/2k_B T)} & \text{for} \quad S_{HR} < l \\ \frac{l}{S_{HR}\sinh(\hbar\omega_\nu/2k_B T)} & \text{for} \quad S_{HR} > l \end{cases}$	(7)
Sommerfeld factor	$s_a = 4(\pi R_H^*/k_B T)^{1/2}$	(8)
Expressions for calculation of Huang-Rhys factor[7]		
Huang-Rhys factor for polar optical coupling	$S_{HR} = \frac{3}{2(\hbar\omega_\nu)^2}\left[\frac{q^2\,\hbar\omega_\nu}{a_0^3\,q_D^2}\left(\frac{1}{\epsilon_\infty}-\frac{1}{\epsilon}\right)\right] I\left(-2{,}2\mu, \frac{q_D a_H^* \upsilon_T}{2}\right)$	(9)

Huang-Rhys factor for optical deformation potential coupling	$S_{\mathrm{HR}} = \frac{1}{2(\hbar\omega_\nu)^2}\frac{\hbar D^2}{M_\mathrm{r}\omega_\nu} I\left(0{,}2\mu, \frac{q_\mathrm{D} a_\mathrm{H}^* \upsilon_\mathrm{T}}{2}\right)$	(10)
Function *I*	$I(\mathrm{a},\mathrm{b},\mathrm{c}) = \frac{1}{(\mathrm{bc})^2}\int_0^1 \frac{y^\mathrm{a}\sin^2(\mathrm{b}\tan^{-1}(\mathrm{cy}))}{[1+(\mathrm{cy})^2]^\mathrm{b}} dy$	(11)
Additional expressions		
Radius of the sphere of the Brillouin zone q_D	$q_\mathrm{D} = \sqrt[3]{6\pi^2}/\mathrm{a}_0$	(12)
Bohr radius a_H	$a_\mathrm{H} = 4\pi\epsilon_0/mq^2$	(13)
Effective Bohr radius a_H^*	$a_\mathrm{H}^* = a_\mathrm{H}\epsilon/m^*$	(14)
Rydberg energy R_H	$R_\mathrm{H} = q^2/(8\pi\epsilon_0 a_\mathrm{H})$	(15)
Effective Rydberg energy R_H^*	$R_\mathrm{H}^* = q^2/(8\pi\epsilon a_\mathrm{H}^*)$	(16)

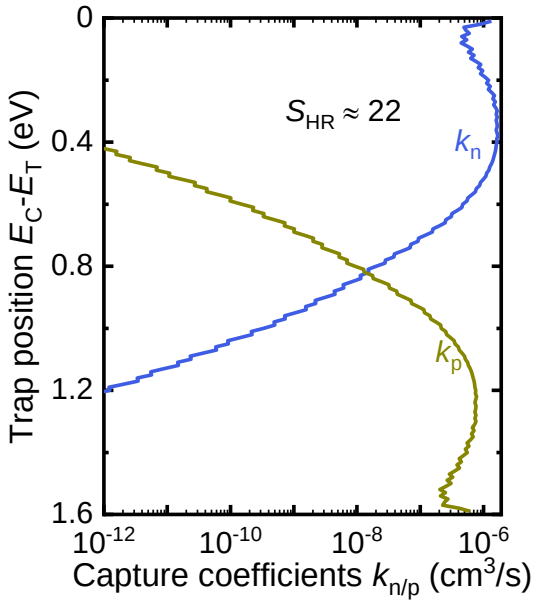

Fig S1: Capture coefficients calculated using arbitrarily chosen values of S_{HR} (same for all energy levels)

Material parameters

All photovoltaic device simulations presented here, were performed using the Advanced Semiconductor Analysis(ASA) software[8,9] , an integrated opto-electronical tool developed by the Photovoltaic Materials and Devices at TU Delft.

To calculate the absorption coefficient values, we used Eq. S1 where E_U is the Urbach energy(band tail), E_g is the bandgap of the perovskite layer and E is the energy of the solar spectrum. We used the absorption coefficient values and an AM1.5G solar cell spectrum as the input to ASA to calculate the carrier generation profile.

$$\alpha = \begin{cases} \alpha_0 \sqrt{\dfrac{E - E_g}{kT}} & for\ E > (E_g + E_U)/2 \\ \alpha_0\, exp\left(\dfrac{E - E_g}{E_U}\right) \sqrt{\dfrac{E_U}{2\, exp(1)\, kT}} & for\ E < (E_g + E_U)/2 \end{cases} \quad (17)$$

Table II Material parameters used in simulation.

Thickness of Absorber ,d_{pero}	300 nm
Thickness of Hole transport layer, d_{HTL}	20 nm
Thickness of Electron transport layer, d_{ETL}	20 nm (Fig. 4, 5, 8a, 9a-b, S1-S3) 50 nm (Fig. 8b, 9c and 9d)
Thickness of interfaces (HTL/Pero , ETL/Pero)	2 nm
Electron affinity of Absorber, $E_{A(Pero)}$	4 eV
Electron affinity of HTL, $E_{A(HTL)}$	2.6 eV 2.5 eV (Fig S1- S3)
Electron affinity of ETL, $E_{A(ETL)}$	4 eV 4.1 eV (Fig S1- S3)
Bandgap of Absorber, $E_{g(Pero)}$	1.6 eV
Bandgap of HTL, $E_{g(HTL)}$	3 eV
Bandgap of ETL, $E_{g(ETL)}$	3 eV
Bandgap of HTL/Pero interface	$E_{g(HTL)} + E_{A(HTL)} - E_{A(Pero)}$
Bandgap of ETL/Pero interface	$E_{g(Pero)} + E_{A(Pero)} - E_{A(ETL)}$
Mobility of Absorber, $\mu_{(Pero)}$[10]	30 cm^2/Vs
Mobility of HTL, ETL $\mu_{(HTL,ETL)}$[11]	10^{-2} cm^2/Vs Fig. 4, Fig.6 Fig. 8, Fig. S2-S4 10 cm^2/Vs Fig. 5 10^{-5} – 10 cm^2/Vs Fig. 9
Effective density of carriers (all layers)	2.2×10^{18} cm^{-3}
Direct recombination coefficient (all layers)	5×10^{-11} cm^3/s
Density of Donor traps (Interface and absorber layers)	10^{15} cm^{-3} Absorber: 5×10^{13} cm^{-3} (Fig. 6b) Interface: 3×10^{9} cm^{-2} (Fig. 6b) 5×10^{17} cm^{-3} (Fig S1,S2) Variable (Fig S3)
Electron capture coefficient (k_n)[1,12]	Variable (Fig. 4 and 5) 0.7×10^{-8} cm^3/s (Fig. 6b, Fig. 8 and 9) 10^{-5} cm^3/s (Fig S1-S3)
Hole capture coefficient (k_p)	Variable (Fig. 4 and 5) 0.2×10^{-4} cm^3/s (Fig. 6b, Fig. 8 and 9) 10^{-9} cm^{-3}/s (Fig S1 - S3)
Urbach energy (E_U)	0.014 eV
α_0	10^{-4} cm^{-1}

Effect of built-in-voltage when device is limited by interface recombination.

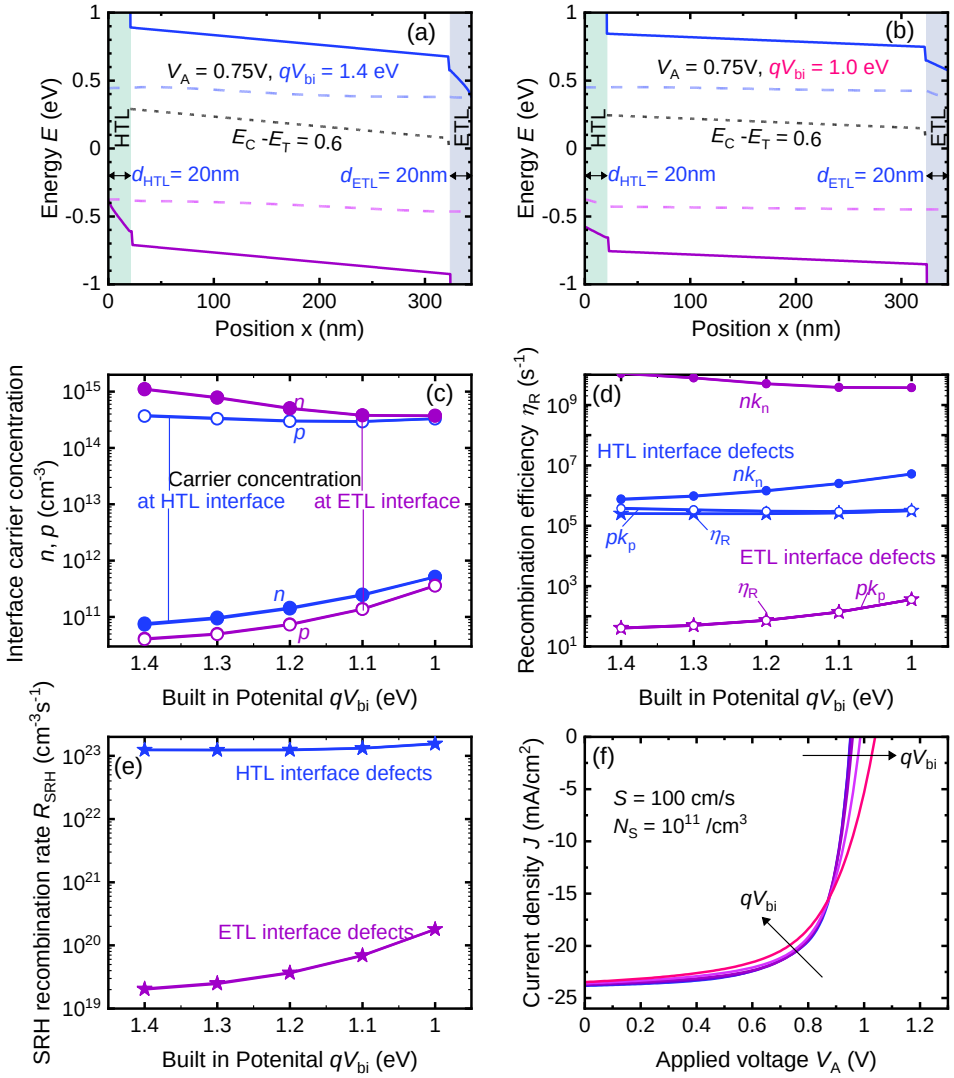

Fig S2 Effect of qV_{bi} in a device limted by interface recombination with a surface recombination belovity of 100cm/s. (a) Band diagram of a symmetric device with a conduction band offset and valence band offset of 0.1eV plotted at an applied voltage V_A = 0.75V with a built-in-potential qV_{bi} = 1.4eV . (b) Band diagram of the same device at a reduced qV_{bi} = 1.0 eV due to introduction of injection barriers at both contacts. (c) Electron concentration n and hole concentration p at the HTL/pero interface in blue and at the ETL/Pero interface in purple for different values of qV_{bi} at V_A = 0.75 V. The filled symbols represent electron concentration and the open symbols represent hole concentration (d) Electron and hole capture rates and the respective recombination efficiency at the HTL/Pero (blue curves) and ETL/Pero (purple curves) interface. The filled circular symbols represent the nk_n and the open symbols represent pk_p values at various values of qVbi at the two interfaces. The respective recombination efficiency at the ETL/Pero interface are represented star symbols. (e) The SRH rate R_{SRH} at the HTL/Pero interface(blue curve) and at the ETL/Pero interface (purple curve). (f) The current voltage curves for different values of $qV_{bi.}$

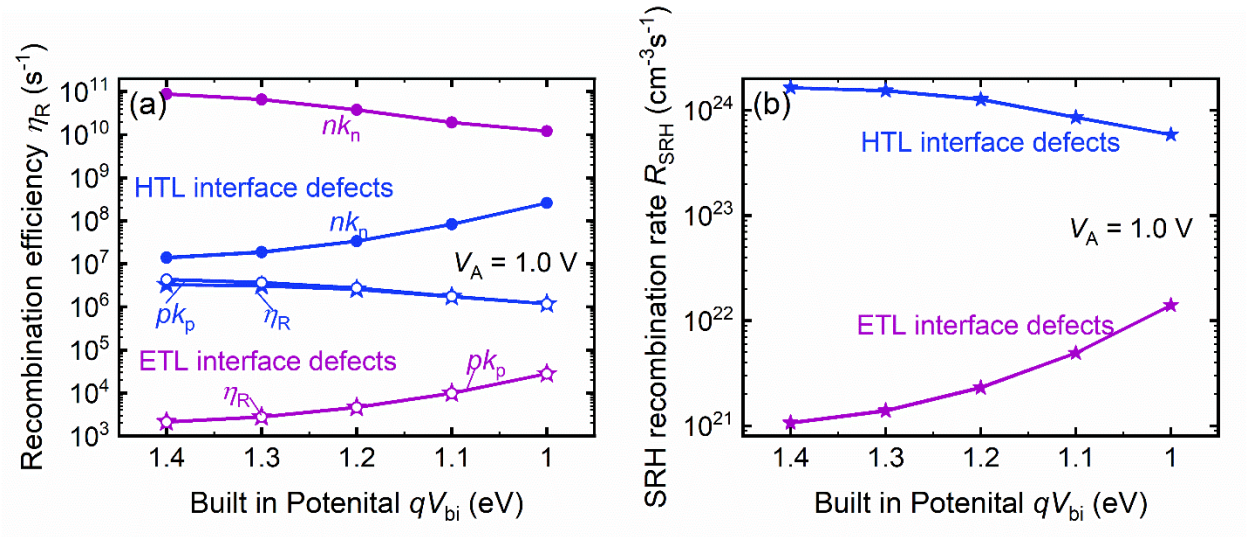

Fig. S3 Capture rates , recombination efficiency and SRH recombination rates at V_A = 1.0 V. (a) nk_n (filled circular symbols) and pk_p (open symbols) at the HTL/Pero in blue and ETL/Pero interface in purple. The respective η_R in star symbols. (b) The SRH recombination rate at the two interfaces for various values of qV_{bi}.

In Fig. S2a and b, we plot the band diagrams of a device with band offset of 0.1eV at both HTL/Pero and ETL/Pero interface at V_A = 0.75V. In Fig. S2a there is no injection barrier and the qV_{bi} = 1.4eV and in Fig. S2b there is an injection barrier of 0.2 eV at both the contacts, thus reducing the qVbi to 1.0 eV. In Fig. S2c , we plotted the electron and hole concentration at the two interfaces for various values of qV_{bi}. The built-in-voltage has little effect on the carrier concentration at the two interfaces. The hole concentration increases very slightly with the change of qV_{bi}. Since the hole capture coefficient $k_p = 10^{-9}$ cm3/s is much smaller than the electron capture coefficient $k_n = 10^{-5}cm^3/s$, the hole capture process is the rate limiting step as seen from Fig. S2d at both the interfaces. The interfaces have a trap density of $N_T = 5 \times 10^{17}/cm^3$, which leads to a surface charge density of $N_S = 10^{11}/cm^2$ at an interface layer thickness of 2nm and a surface recombination velocity $S = k_p \times N_s = 100$ cm/s. The recombination efficiency then leads to the SRH recombination rates shown in Fig. S2e and the device is limited by defect mediated recombination at the HTL/pero interface. Fig. S2f shows the *JV* characteristics of the solar cell at various values of qV_{bi}. The overall efficiency of the device decreases slightly with decrease of the built-in-potential due to the small increase in the recombination rate at both the interfaces owing to the slight increase in the hole concentration at the two interfaces. Thus, as discussed in the main paper, even very small increase in the carrier concentration associated with the rate limiting step (here pk_p), increases recombination through the defect level and thus reducing efficiency. However, unlike in the device limited by bulk recombination, the open circuit voltage V_{oc} increases in the device discussed here. The improvement in the V_{oc}, can be associated with the decrease in the hole capture rate and thus recombination efficiency at the HTL/Pero interface around the $V_A \approx V_{OC}$ as shown in Fig. S3a. Due to the decrease in recombination efficiency, the associated SRH recombination rate at the HTL/Pero interface also decreases as shown in Fig. S3b. So, once again, the importance of the device geometry in determining the recombination through the defect levels and thus the overall

performance of the device becomes evident from the discussion above. It also highlights the importance of research in determining the dominant defect levels and their capture coefficients in novel materials for improving device performances.

Effect of surface recombination velocity on device performance

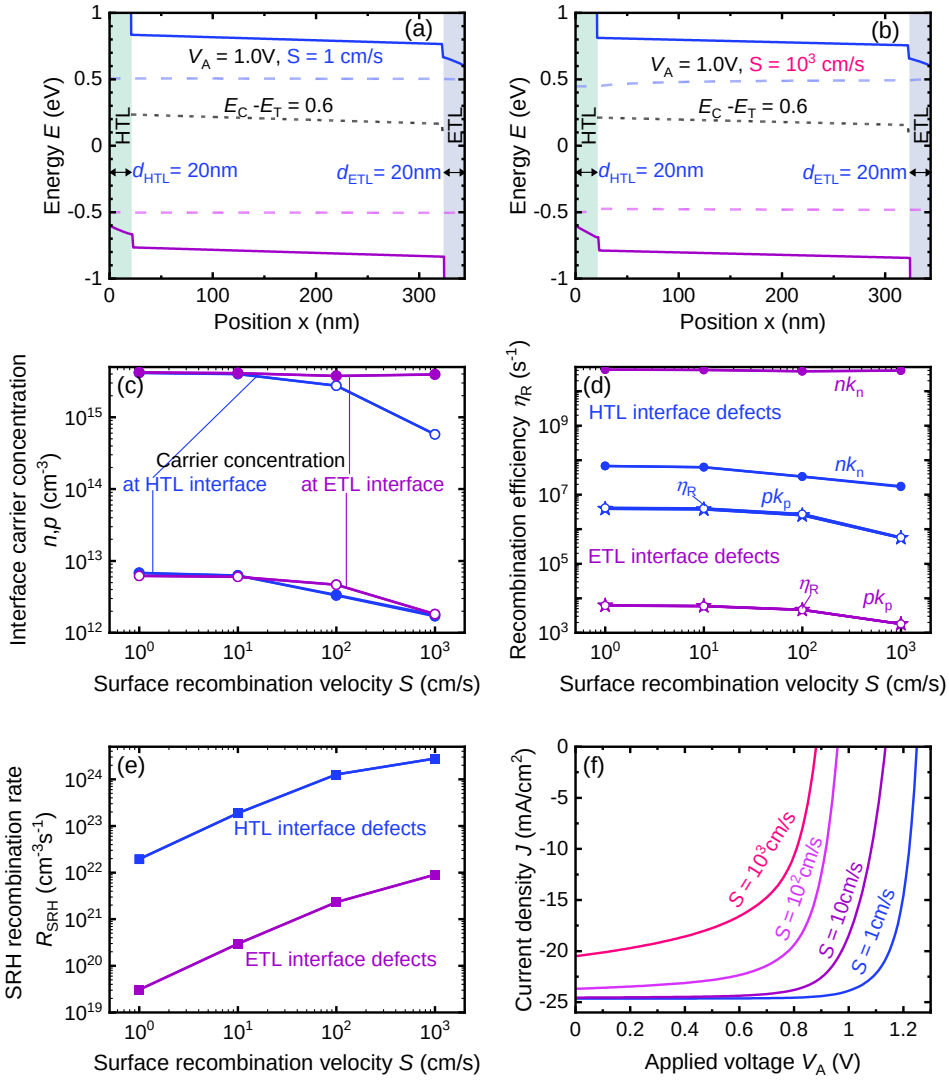

Fig. S4 Effect of surface recombination velocity on devices. (a) Band diagram of a device with surface charge recombination velocity S=1 cm/s. (b) Same as before but with S = 10^3 cm/s. (c) The electron and hole at the HTL/pero and ETL/pero interface for different values of S. The filled symbols represent electron concentration and the open symbols represent hole concentration. (d) The capture rates and recombination efficiency of the defects at the HTL/pero interface are represented in blue and the one in purple represent the respective quantities at the ETL/pero interface. The filled circular symbols represent nk_n and the open symbols represent pk_p. The filled stars represent the respective recombination efficiencies.

In Fig. S4a we plot the band diagram of a device with surface recombination velocity S = 1 cm/s and in Fig. S4b we plot that for a device with S = 10^3 cm/s. In Fig. S4c we plot the values of electron and hole carrier concentration at the two interfaces for different values

of *S*. The electron and hole concentration is shown by blue filled and open symbols, respectively, at the HTL/pero interface. Both carrier concentration at the HTL/pero interface decreases as we increase the surface recombination velocity, by increasing the surface defect density, due to increased recombination at the interface. The electron concentration (filled purple symbols) at the ETL/pero interface decreases slightly as a result of the increase of surface recombination velocity. The hole concentration(open purple symbols) at the ETL/ Pero interface also decreases due to increased recombination. However, when we look at Fig. S4d, we see that the recombination efficiency decreases with increase in S. However, this is logical since at both the interfaces, the hole concentration decreases thus decreasing the hole capture rate. The hole capture rate is the rate limiting step in this device with a defect level characterized by $k_p = 10^{-9}$ cm^3/s and $k_n = 10^{-5}$cm^3/s. However, even though the recombination efficiency decreases through an individual defect, the total recombination rate increases by orders of magnitude due to the increase in surface defect density, as shown in Fig. S3e. As a result of the increase of surface recombination the performance of the solar cell worsens upon increasing the surface recombination velocity.

1 B. Das, I. Aguilera, U. Rau and T. Kirchartz, *Phys. Rev. Mater.*, 2020, **4**, 024602.

2 B. K. Ridley, *J. Phys. C Solid State Phys.*, 1980, **13**, 2015–2026.

3 B. K. Ridley, *Quantum Processes in Semiconductors*, Oxford Science Publications, 5th edn., 2013.

4 T. Markvart, *J. Phys. C Solid State Phys.*, 1981, **14**, L895.

5 T. Kirchartz, T. Markvart, U. Rau and D. A. Egger, *J. Phys. Chem. Lett.*, 2018, **9**, 939–946.

6 P. T. Landsberg, *Recombination in semiconductors*, Cambridge University Press, 1st edn., 1991.

7 B. K. Ridley, *Solid. State. Electron.*, 1978, **21**, 1319–1323.

8 B. E. Pieters, J. Krc and M. Zeman, in *Conference Record of the 2006 IEEE 4th World Conference on Photovoltaic Energy Conversion, WCPEC-4*, IEEE Computer Society, 2006, vol. 2, pp. 1513–1516.

9 ASA simulator, https://asa.ewi.tudelft.nl/, (accessed 22 October 2020).

10 L. M. Herz, *ACS Energy Lett.*, 2017, 2, 1539–1548.

11 V. M. Le Corre, M. Stolterfoht, L. Perdigo, M. Feuerstein, C. Wolff, H. J. Bolink, D. Neher and L. Jan Anton Koster, *Cite This ACS Appl. Energy Mater*, 2019, **2**, 6280–6287.

12 X. Zhang, M. E. Turiansky, J.-X. Shen and C. G. Van De Walle, *Phys. Rev. B*, , DOI:10.1103/PhysRevB.101.140101.